J Mater Sci (2024) 59:5831–5853

Processing Bulk Nanostructured Materials

Recrystallization of bulk nanostructured magnesium alloy AZ31 after severe plastic deformation: an in situ diffraction study

Klaus-Dieter Liss[1,*], Jae-Kyung Han[2], Malte Blankenburg[3], Ulrich Lienert[3], Stefanus Harjo[4], Takuro Kawasaki[4], Pingguang Xu[5], Eitaro Yukutake[6], and Megumi Kawasaki[2,*]

[1] *School of Mechanical, Materials, Mechatronic and Biomedical Engineering, University of Wollongong, Wollongong, NSW 2522, Australia*
[2] *School of Mechanical, Industrial and Manufacturing Engineering, Oregon State University, Corvallis, OR 97331, USA*
[3] *DESY Photon Science, Deutsches Elektronen-Synchrotron, 22607 Hamburg, Germany*
[4] *J-PARC Center, Japan Atomic Energy Agency, Tokai, Ibaraki 319-1195, Japan*
[5] *Materials Sciences Research Center, Japan Atomic Energy Agency, Tokai, Ibaraki 319-1195, Japan*
[6] *Industrial Technology Innovation Center of Ibaraki Prefecture, Higashiibaraki-gun, Ibaraki 311-3195, Japan*

Received: 4 November 2023
Accepted: 6 December 2023
Published online: 17 January 2024

© The Author(s), 2024

ABSTRACT

The magnesium alloy AZ31, which has undergone high-pressure torsion processing, was subjected to in situ annealing microbeam synchrotron high-energy X-ray diffraction and compared to the as-received rolled sheet material that was investigated through in situ neutron diffraction. While the latter only exhibits thermal expansion and minor recovery, the nanostructured specimen displays a complex evolution, including recovery, strong recrystallization, phase transformations, and various regimes of grain growth. Nanometer-scale grain sizes, determined using Williamson–Hall analysis, exhibit seamless growth, aligning with the transition to larger grains, as assessed through the occupancy of single-grain reflections on the diffraction rings. The study uncovers strain anomalies resulting from thermal expansion, segregation of Al atoms, and the kinetics of vacancy creation and annihilation. Notably, a substantial number of excess vacancies were generated through high-pressure torsion and maintained for driving the recrystallization and forming highly activated volumes for diffusion and phase precipitation during heating. The unsystematic scatter observed in the Williamson–Hall plot indicates high dislocation densities following severe plastic deformation, which significantly decrease during recrystallization. Subsequently, dislocations reappear during grain growth, likely in response to torque gradients in larger grains. It is worth noting that the characteristics of unsystematic scatter differ for dislocations created at high and low temperatures, underscoring the strong temperature dependence of slip system activation.

Handling Editor: M. Grant Norton.

Address correspondence to E-mail: kdl@uow.edu.au; liss@kdliss.de; megumi.kawasaki@oregonstate.edu

https://doi.org/10.1007/s10853-023-09250-4

GRAPHICAL ABSTRACT

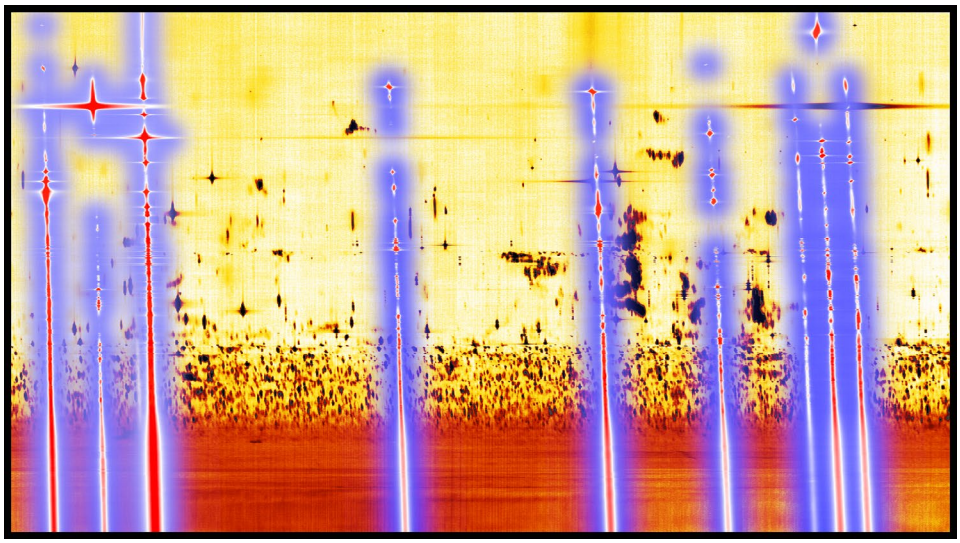

Proem on nanostructured materials and in situ techniques

The thermal stability of bulk nanostructured materials, as obtained by severe plastic deformation, continues to be a subject area of ongoing research. Their ultrafine grain arrangements are far out of thermodynamic equilibrium and expose heterogeneous microstructures. Some of them may already be aged at room temperature, while a minute knowledge of the atomistic recovery and recrystallization processes opens a design route for even harder nanostructured materials than those without post-deformation heating [1]. Here we report on in situ studies of such structural behavior and evolution by exploiting microbeam high-energy synchrotron diffraction complemented by in situ neutron scattering. With the readiness of bulk-penetrating radiation, synchrotron high-energy X-rays [2] and neutrons [3], in situ studies became routinely available to investigate the phase and microstructural evolution in real time, in situ upon applying a temperature ramp.

High-pressure torsion has been particularly employed to design and process heterogeneous metals and compounds with enhanced mechanical properties or unexpected functional behavior. For example, aluminum has been mechanically alloyed with magnesium resulting in supersaturated alloys with a Vickers hardness increase from 65 to 340 [4, 5]. This specific alloy was further characterized by submillimeter high-energy synchrotron X-ray diffraction for displaying the position-sensitive, thus shear strain-dependent, phase transformation, which occurred during the high-pressure torsion induced mechanical alloying [6]. Interestingly, nanostructured CoCrFeNi high-entropy alloy not only shows hardness increase with grain refinement [5] but moreover unexpected magnetic response through spin clustering [7]. Its high-temperature microstructural evolution has been investigated by in situ neutron diffraction, showing regimes of stress recovery, recrystallization, and followed by grain growth [8]. The results from the in situ heating experiments benefit the visualization of continuous events of microstructure and defect evolution, which supports the consequences of the changes in mechanical responses of similar nanostructured high-entropy alloys after annealing [9]. Altogether, novel in situ and microbeam studies using synchrotron and neutron radiation as well as high-temperature laser scanning confocal microscopy allow probing for local, bulk and high-temperature states of the microstructure and its evolution, opening a playground of tools for determining in detail atomistic constellations and mechanisms of change [10, 11].

Magnesium alloys are of particular interest, generally because of their lightweight, but also because of their corrosion properties, e.g., when engineering self-dissolving medical implants [12, 13]. Nanostructurization by high-pressure torsion at room temperature has

increased the Vickers hardness of common Mg alloys from ~ 60 to ~ 110–120 [14], leading to the enhancement in mechanical strength that attracts further the application of Mg alloys as innovative biodegradable materials [15] even if the corrosion resistance is improved together by homogenization of microstructure and chemical distribution. After severe plastic deformation, the above-mentioned lightweight aluminum and magnesium alloys have shown aging at room temperature [4]; thus, the investigation of thermal stability and microstructure evolution is a necessary aspect for materials design. Particularly in situ studies on magnesium alloys have shown interesting features that are difficult to reveal by conventional methods: In situ monochromatic high-energy X-ray diffraction upon the thermal transformation behavior and microstructural evolution of both AZ91 and AZ31 alloys at high temperature revealed thermal expansion coefficients and their anomalies due to the dissolution of intermetallic phases and grain growth effects [16]. A plastic compression experiment of AZ31 under synchrotron radiation at different temperatures not only shows recovery and dynamic recrystallization but also reveals the plastic deformation mechanisms, including twinning at room temperature and switching to sequentially activated slip systems at high temperatures [17, 18]. Moreover, a recent white-beam Laue study demonstrates the reorientations of grains in AZ91 at high temperatures, solving the missing puzzle stone for the initiation of abnormal grain growth by spontaneous activation of diffusion at grain boundaries [19].

Microstructure-related observations are based on a relatively small number of grains within the illuminated volume, such that reflections from individual grains can be spotted on the diffractograms. The powder diffraction method, as conventionally applied to polycrystalline materials, requires a sufficiently large number of diffracting grains in order to illuminate the Debye–Scherrer rings homogeneously, while any distinguished single-grain reflection can falsify the intensity readings. The above-mentioned novel methods make use of the graininess of the material, where individual reflections can be distinguished and followed in their evolution in a halo of many others [20]. For nanocrystalline structures, however, the number of grains in an illuminated volume defined by say a 500 × 500 μm^2 wide beam becomes too large to be resolved. Therefore, in order to follow single-grain reflections in a nanocrystalline material, the beam size needs to be scaled down accordingly. Taking this into consideration, the current paper presents a novel in situ heating experiment employing a microfocused high-energy synchrotron beam on nanostructured magnesium AZ31. Simultaneously, for comparison purposes, bulk studies are being conducted on the conventional as-received material through in situ neutron scattering. The implemented techniques demonstrated in this report provide important insights into the microstructural transitions over temperature and time. The obtained knowledge offers the keys to understanding the relaxation behavior of severely deformed nanostructured metals in a wider sense.

The magnesium specimen system

Rolled sheets of the magnesium alloy AZ31 have been provided by the Ibaraki Prefectural Industrial Technology Center. The nominal composition of AZ31 is Mg-3Al-1Zn in mass-%, and it has been experimentally determined by Liu et al. [16] to be Mg-2.7Al-1.1Zn-0.4Mn (mass-%), translating to Mg-2.45Al-0.41Zn (at.%). Pieces measuring 30 mm in the rolling (RD), 10 mm in the transverse (TD), and 2 mm in the normal direction (ND) were employed for neutron scattering. Additionally, 10-mm-diameter disks were processed by high-pressure torsion under 6 GPa, 15 turns, and 1 rpm at room temperature using a Moinsys HPT System from South Korea, equipped with a press unit of 1 MN force. A quarter of the resulting 0.9-mm-thick disk was used for the microbeam synchrotron study.

Neutron scattering for the as-received sheet

In situ neutron diffraction has been undertaken on the as-received sheet material undergoing a temperature profile, heating from room temperature by 0.2014 K/s to 700 K, held for 1770 s, and subsequently furnace-cooled. We used the Takumi (匠) diffractometer at beamline BL19 [21] of the Materials and Life Science Experimental Facility (MLF), at the Japan Proton Accelerator Research Complex (J-PARC) [22, 23]. The dilatometer furnace, heated by halogen lamps, has been used with the specimen oriented 45° to the incident beam, such that the RD and ND components are probed in the North (北) and South (南) detector banks, 0000 and 0001, respectively [24]. The experiment was conducted during the beam time 2014A0267,

which is identical to another experimental run published earlier [25], to which readers can refer regarding instrument settings and calibration. The present study is identified by the dataset 5347, run number ENG022681, and the logbook entry for the specimen is S08-Mg-AZ31.

The event data have been histogrammed into 211 time bins, each of 30 s in order to allow for acceptable counting statistics, and single peaks were fitted by Gaussians in time-of-flight space using the Igor Pro 4 software to the Mg-100, Mg-101, Mg-110, Mg-200, Mg-112, Mg-201 reflections in RD and Mg-002, Mg-101, Mg-102, Mg-103 in ND. Subsequently, all results were converted to the reciprocal space scale in units of the scattering vector [3].

Synchrotron microbeam diffraction for nanostructured material

To probe for grain-resolved diffraction, we exploit microbeam high-energy synchrotron radiation, in situ and time-resolved upon a heating ramp, driving heat from room temperature by 0.1655 K/s to 876 K. The experiment has been carried out at the PETRA-III beamline P21.2 at DESY [26] under proposal number I-20200639. A monochromatic X-ray energy has been tuned to 61.7 keV for focusing the beam by 84 composite refractive lenses to the specimen at about 2160 mm downstream and an effective aperture of 252 µm. The vertical focus size was reported to be 2.4 µm and about double horizontally, illuminating a cross section of about 3×6 µm^2. This fixes the incident wave vector to $k = 31.27$ Å^{-1} [3]. Two flat panel detectors of type VAREX XRD 4343CT were positioned downstream right and left to the transmitted beam, with *short* and *long* camera lengths of 902 mm and 2192 mm, respectively. Each detector possesses 2880×2880 pixels of size 150×150 µm^2, which gives an excellent azimuthal resolution. The two detector settings result in larger reciprocal space coverage at short and better resolution at longer distances [2, 27]. The camera lengths of the detectors have been obtained by triangulation by sample translation along the beam while the wave number has been verified by a LaB_6 standard.

Data recording rates for the short and long camera detectors have been 2 Hz and 1 Hz, respectively, leading to 6925 and 3462 two-dimensional diffractograms.

A Linkam THMS600 enclosed micro-oven comprising a disk-shaped flat resistive heater made of boron nitride with a central hole for beam transmission has been used to adjust the temperature under argon atmosphere. The specimen was stuck by thermal conductive paste to its downstream surface, covering the hole, such that the beam was transmitted through the specimen along its normal. The beam position on the high-pressure torsion specimen was close to the center of the disk quarter, therefore more than half radius out from the center of the original torsion disk. With 15 turns of processing, this assures that we probe in a saturated volume of nanostructurization by severe plastic deformation (Fig. 1).

For data reduction, we use the scilab-6 based *dataRring* scripts allowing for sectorizing the diffractograms, and extracting both radial and azimuthal coverage of reciprocal space [16, 17, 20]. For the first time, we used as many as 2880 sector divisions of a full diffraction ring, resulting in an azimuthal binning width of 0.125°. Radial single-peak fitting has been undertaken for a series of the Laue–Bragg interferences Mg-100, Mg-002, Mg-101, Mg-102, Mg-110, Mg-103, Mg-112, Mg-201, Mg-211, using Gaussian fitting in *dataRring*.

The logbook entry at this run under beam time I-20200639 is 'Sample 8.'

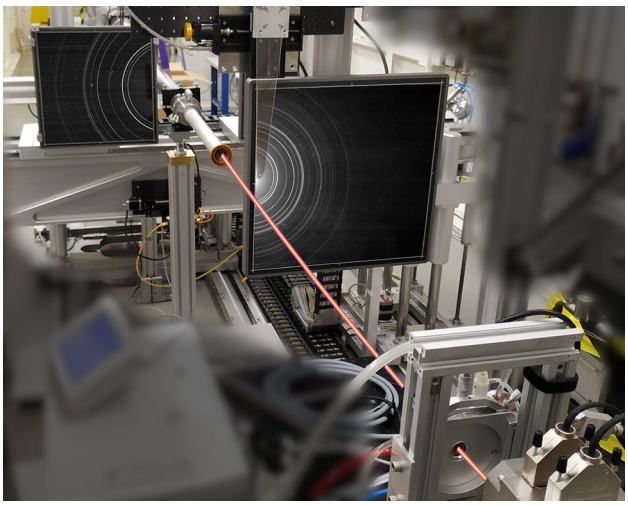

Figure 1 Photomontage of setup at DESY, the beam arriving from the bottom right and propagating up left, and diffractograms on the two detectors with short camera length (right) and long (left).

Observations during heating of the as-received material

The overall diffractograms are displayed in Fig. 2 for the as-rolled AZ31 alloy with orientations of the scattering vector (upper) along the rolling direction RD (0000) and (lower) along the normal direction ND (0001). The color-coded diagrams expose profound lines of the *hcp* structure of magnesium with space group designation $P\,6_3/m\,m\,c$. The peaks strongly react to the heating profile by shifting to the left at higher temperatures due to thermal expansion. Some faint lines can be seen at 2.7695, 3.1928, and 4.5115 $Å^{-1}$, responding much less to the temperature change, matching an $I\,m\,\bar{3}\,m$ space group with a lattice parameter of 3.9348 Å. This phase has to be stable over the temperature range as it does not show any evolution, apart from thermal expansion. We ascribe it to aluminum oxide by the entry #1010461 of the Crystallography Open Database (COD), which indeed has a much smaller thermal expansion coefficient [28] and disregard it for further analysis due to its inert stability. Lattice expansion of the *hcp* Mg phase becomes apparent when plotting the total lattice strain, i.e., the relative change in lattice plane distance, against temperature, as evaluated for all fitted neutron reflections as shown in Fig. 3. All superimposed reflections are well consistent within the experimental accuracy at any temperature, stating isotropic thermal expansion as revealed and discussed in the literature [29, 30]. Besides the fact that the temperature reading of this furnace chronologically lags behind the sample temperature [25], the curves show fully linear behavior and equal slope for heating and cooling, resulting in a thermal expansion coefficient of $31.1{\cdot}10^{-6}$ K^{-1}. The observed value and isotropy are consistent with independent studies in the literature. While the expansion values of pure magnesium single

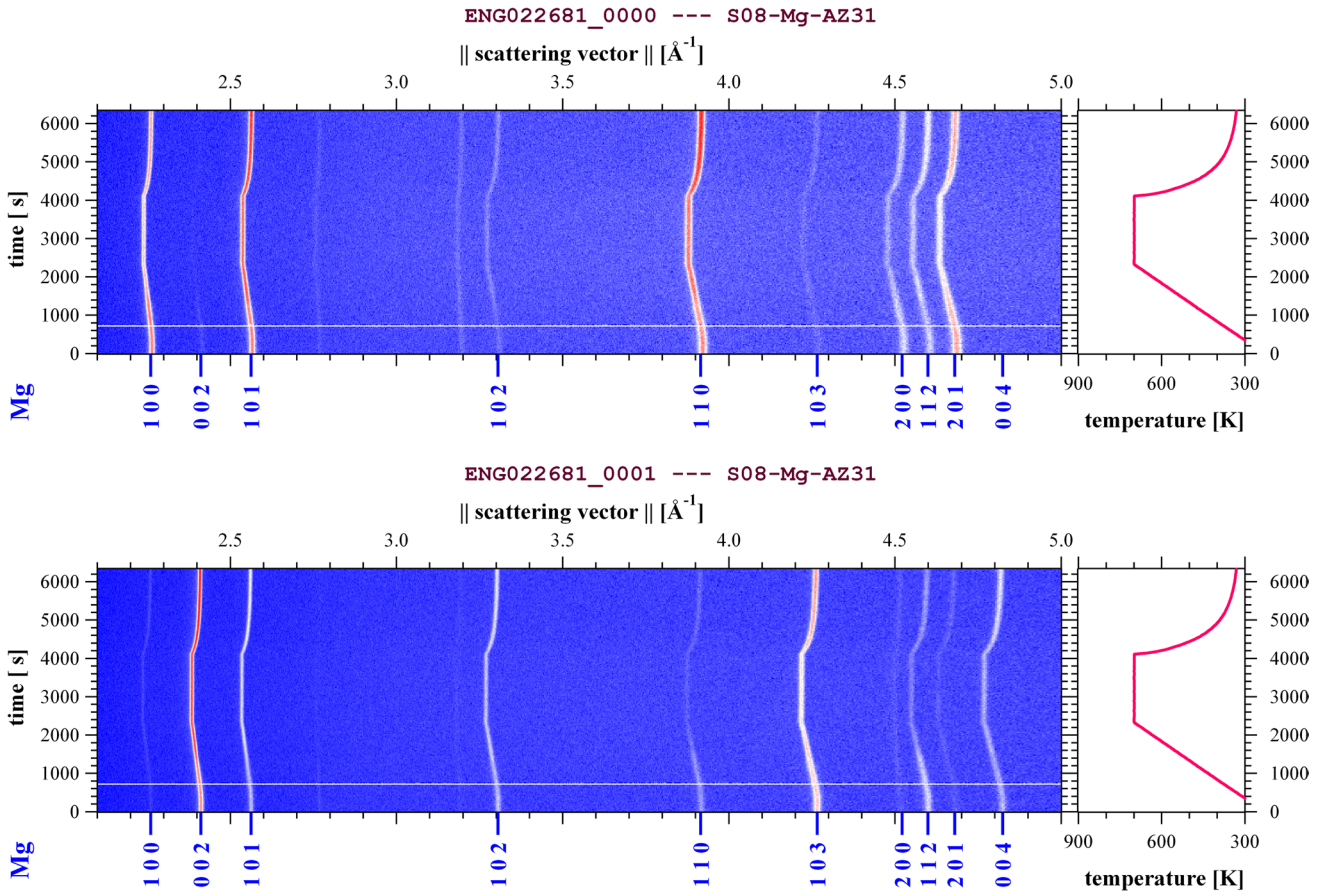

Figure 2 Overall neutron diffractograms of as-received sheet AZ31 with orientations of the scattering vector along the rolling direction RD (0000) and normal ND (0001) with intensity in color-code along the modulus of scattering vector and time. Blue represents low, white medium and red high intensity. The temperature profile run is shown to the right.

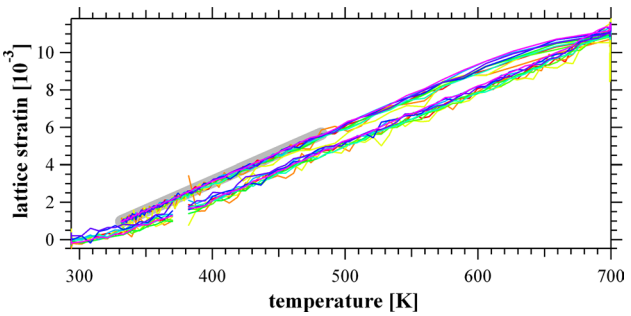

Figure 3 Lattice strain versus temperature for the as-received sheet material, evaluated for all fitted neutron reflections. The curvature at low and high temperatures is due to a lag between applied and read values. The thick gray line is fitted to the lower temperature branch upon cooling with a slope of $31.1(1)\cdot10^{-6}$ K^{-1}.

crystal lie a little lower, as reviewed by Childs [29], measurements on AZ31 reveal similar augmented values to ours, obtained from the same sheet material by synchrotron high-energy X-ray diffraction and using a different furnace [16]. Indeed, the literature states true thermal expansion coefficients of magnesium alloys range between $26\cdot10^{-6}$ K^{-1} and $32\cdot10^{-6}$ K^{-1} [31].

The evolution of the peak widths with heating followed by cooling is displayed in Fig. 4 for the Mg-100 and Mg-101 reflections of the alloy in RD (left), together with a Williamson–Hall plot for the sample at the starting and ending conditions (right). The gray line is the slope of the resolution function taken from the sister experiment [25]. The reduction in the peak width reveals some recovery of the rolled microstructure, which seems to hit the baseline at around 550 K upon heating. The axes offsets of the linear Williamson–Hall regression scatter around zero and are therefore meaningless, because grain sizes are already in the micrometer range in the starting condition and throughout the experiment. For such large grains, the Williamson–Hall method fails because of extinction effects and is therefore not applicable for grain size determination. The slope of the regression significantly diminishes demonstrating well the disappearance of lattice strain gradients. Thus, peak broadening and its change origins in the microstrain rather than from grain size. The difference between the fitted slope and that of the resolution function results in a microstrain of $1.6\cdot10^{-3}$ in the as-received rolled sheet material before heating and reduces to $0.5\cdot10^{-3}$ reaching 700 K upon heating. Upon further holding at 700 K

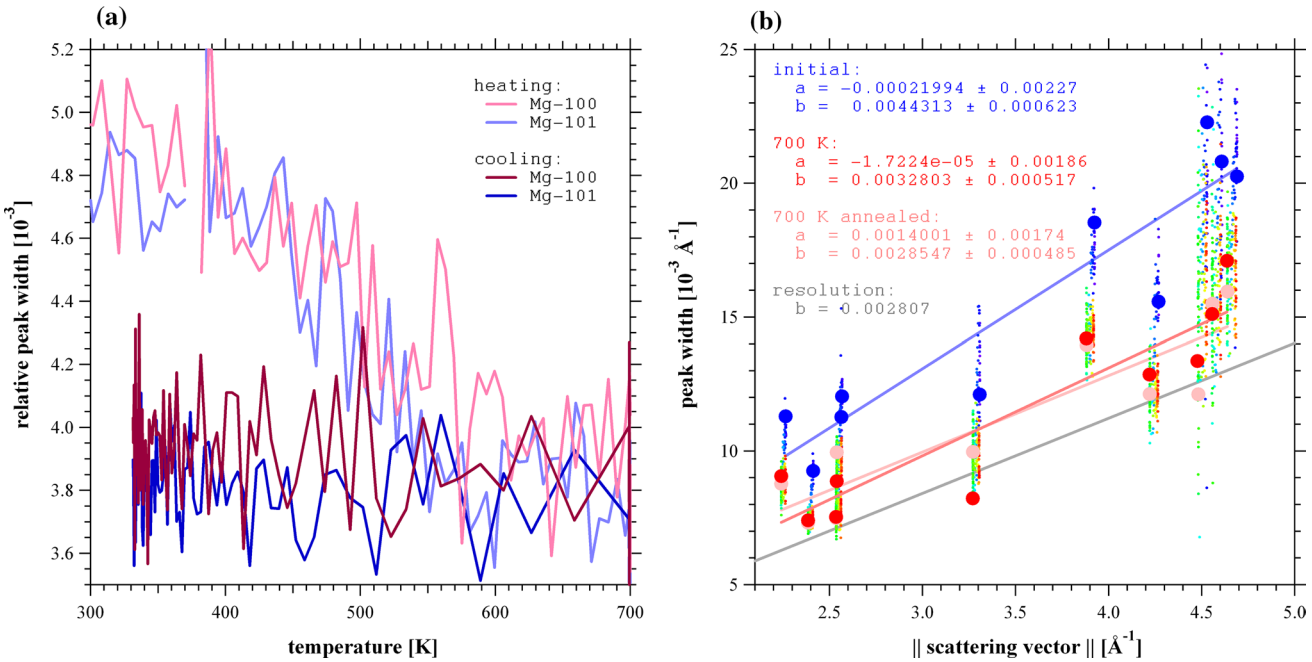

Figure 4 Temperature evolution of relative peak widths $\Delta G/G$ of the selected Mg-100 and Mg-101 reflections in RD (**a**) and Williamson–Hall plot presenting width ΔG versus scattering vector G, containing all fitted peaks and their temporal evolution coded in rainbow colors (**b**). The starting and high-temperature conditions have been emphasized by blue and red markers, respectively, and straight lines fitted, with the displayed regression parameters.

for 1230 s, the microstrain decreases below $0.1{\cdot}10^{-3}$ showing stress relaxation and chemical homogenization upon annealing. The unsystematic scatter, however, prevails and evolves only slowly, testifying to persisting dislocation densities.

Last but not least, there is pronounced texture in the as-received material as seen from the very weak peaks Mg-002 in the RD, as well as weak Mg-100 and Mg-110 in ND diffractograms (see Fig. 2). Thus, the (002) plane normal is parallel to the sheet surface normal, while both the (100) and (110) plane normals align with the rolling direction. This represents the typical magnesium basal texture for rolling in a high degree of fiber configuration. Similar interpretations have been made on extruded magnesium AZ31 by Harjo et al. [32]. Our result on the as-received sheet texture is consistent with the synchrotron high-energy X-ray measurements of Liu et al. [16] of the same batch material, as well as with generic texture reports by the manufacturing institute [33].

Microbeam diffraction results of high-pressure torsion-processed material

A few representative two-dimensional detector images are shown in Fig. 5 displaying Debye–Scherrer rings with the overall coverage of the high-pressure torsion-processed Mg AZ31 alloy (upper) and at the selected sections showing three inner rings with Miller indices Mg-100, Mg-002, and Mg-101 (lower), where these are taken through long and short camera lengths at given experiment times and temperatures. At lower temperatures, as represented at 320 K, the diffraction rings are continuous and smooth proofing for a grain size much smaller than the illuminated gauge volume of $V_g = 16{\cdot}10^3$ μm^3. Typical grain sizes of magnesium after high-pressure torsion are 0.1 μm resulting in $N_s = 16{\cdot}10^6$ scattering grains, each of them having a large mosaic spread, i.e., subgrain orientation distribution, making up the smooth rings. The display at 445 K reveals already diffraction spots from individual grains, meaning that grains have recovered and grown. On the long camera and the Mg-100 ring, we estimate a separation between spots of 3 pixels by a ring radius of 2655 pixels, corresponding to a separation of $\delta = 0.065°$. Their mosaic spread is the azimuthal width of each reflection and estimates $\eta = 0.03°$. Then, the number of grains in the illuminated volume can be estimated by $N_s = 4\pi/\delta^2{\cdot}\delta/\eta/N_m/\cos(\theta) = 3.5{\cdot}10^6$, where 4π is the full-sphere solid angle, $N_m = 6$ is the multiplicity of the Mg-100 reflection, and $\cos(\theta) = (1 - G^2/4k^2)^{½}$ is the cosine of the Bragg angle θ at scattering vector G, resulting in a grain size of $D = (V_g/N_s)^{1/3} = 166$ nm.

Another probe is shown in Fig. 5 at 527 K where spot separations at the long camera may reach 25 pixels, thereby scaling the grain size into the 1.4 μm range.

The preceding derivation is a very rough estimate that may need further investigation; however, the takeaway is that we start from ultrafine grains that show a large amount of defects, thus a large mosaic spread, covering smoothly the Debye–Scherrer rings. Upon continuous heating to 445 K, the grain size has increased, and the mosaic spread has been reduced to the order of the instrument resolution, thus more perfect grains with significantly reduced dislocation densities. This high instrument resolution with microbeam optics allows for the observation of single-grain reflections on the 166 nm scale, which is not possible with conventional techniques. The evaluated numbers make perfect sense with respect to the results obtained by Malheiros et al. [34], keeping in mind that X-ray and neutron diffraction are more sensitive to subgrain formations, leaning toward smaller grain sizes. Fingerprints of such subgrain configurations are the broad azimuthal distributions observed, e.g., in Fig. 5 at 527 K on the Mg-100 ring.

Regarding the texture, small variations are seen at 320 K on the second inner ring, the Mg-002 Laue–Bragg interference. The fact that the scattering vector of this reflection appears in the disk radial direction means that the initial sheet texture with Mg-002 along ND has been largely reset. This is consistent with earlier observations that the final high-pressure torsion texture does not inherit any as-received starting texture [35]. There is a variation on the Mg-002 ring depending on the local shear direction during processing, see e.g., [4], which cannot be quantitatively evaluated as the sample has been oriented randomly in azimuth.

Azimuthal perspective of reciprocal space: orientation distribution of grains

The so-called azimuth–time plots were introduced by Liss and co-workers [20] as a powerful analytical method for illuminating the behavior of separate grains in polycrystalline metals, i.e., slip deformation

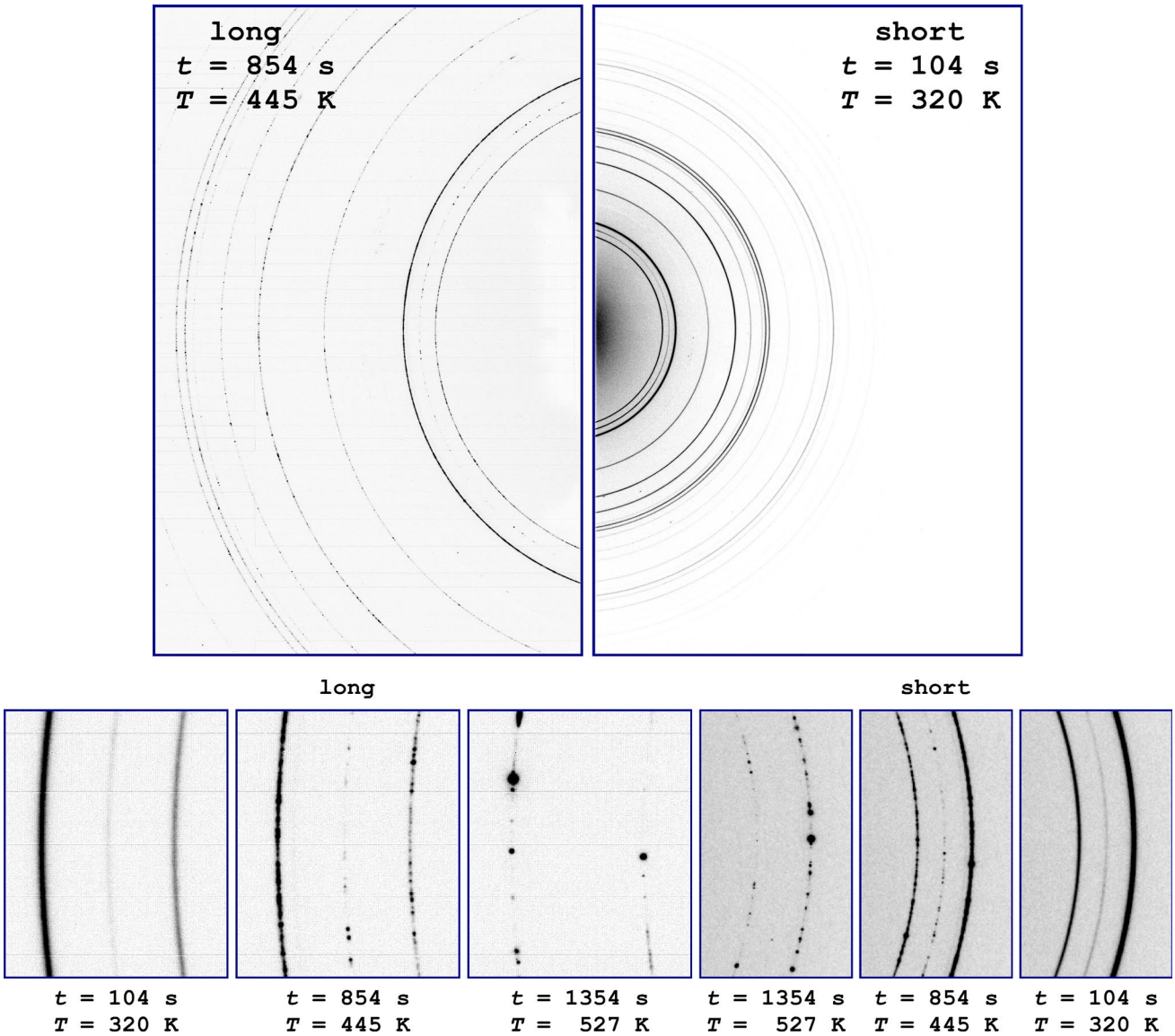

Figure 5 Detector images of long and short camera lengths at given experiment times and temperatures. The top row shows the overall coverage, followed by zoomed extracts of the first three inner rings around the vertical centerline, with Miller indices Mg-100, Mg-002, and Mg-101 at radii 2.26 $Å^{-1}$, 2.41 $Å^{-1}$, and 2.56 $Å^{-1}$, respectively.

in copper at room temperature [36], dynamic recovery and recrystallization in zirconium alloy at high temperatures [37], and deformation and annealing processes in magnesium alloys [16, 17]. Figure 6 shows the azimuth–time plots for Miller indices Mg-100, where the plot covers (a) the entire duration of the experiment and (b) a specific region of interest in time at which recrystallization occurs. In principle, for each time step, the intensity distribution on a given Debye–Scherrer ring is represented as a horizontal line against the azimuth on the abscissa, which is spread out over time on the ordinate.

Figure 6 shows a few characteristic appearances, namely a gray shaded area with little contrast variation up to 405 K, a transition from then on to 427 K resulting in a sustained mottled distribution, and a sharp transition at 510 K to areas with sparse reflections.

The smooth, gray shaded areas below 405 K correspond to the continuous diffraction rings of the initial ultrafine-grained microstructure processed by high-pressure torsion. As already discussed, grain sizes are

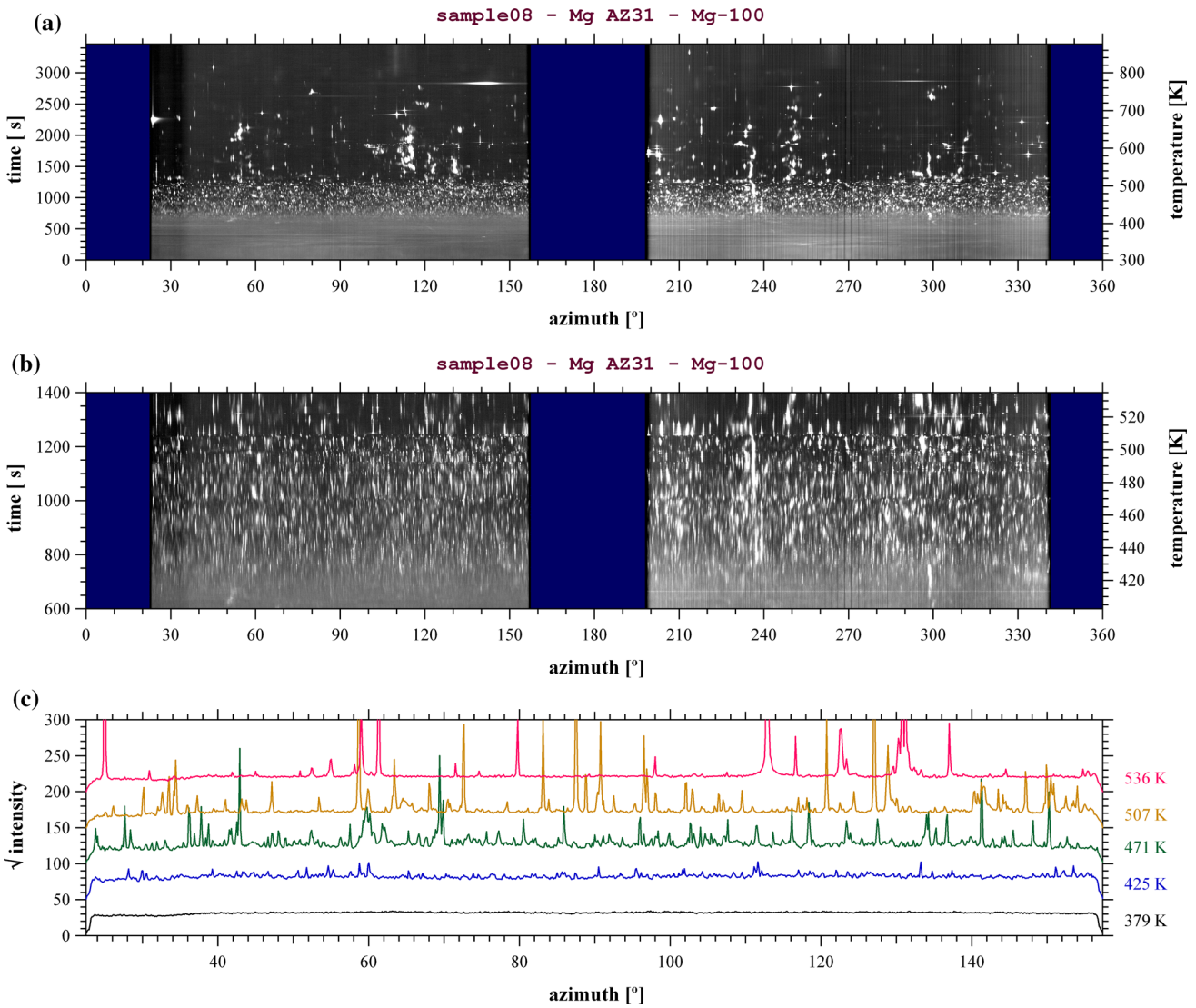

Figure 6 Azimuth–time plots of the Mg-100 reflection (refer to Fig. 7), corresponding to the innermost diffraction ring in Fig. 5. The intensity distribution on this ring is plotted against the azimuth on the abscissa, while the ordinate represents the time evolution, which, in this experiment, correlates monotonically with temperature. Data on the left and right in the figure originate from two detectors with long and short camera distances, respectively. Figure **a** displays the entire duration of the experiment, while **b** zooms in on the region of interest where recrystallization occurs. **c** shows representative line snapshots at selected temperatures.

in the 0.1 μm range, and each grain exposes a large mosaic spread, i.e., numerous low-angle subgrain boundaries, whose distribution can vary by several degrees. This is underlined by azimuthal intensity variations showing texture and blurred regions of higher or lower intensity.

The transition between 405 and 427 K shows emerging sharp intensity spots, first appearing on top of the smooth background, which then augment in contrast. This is the regime of recrystallization, where sharp spots evolve from perfect crystallites, eating away more and more at the volume of the highly distorted material, thus ceasing the smooth background. This mottled distribution prevails over the observed azimuth angle up to 520 K, a range at which the microstructure fluctuates but stays relatively stationary without rapid grain growth. As we will see, the microstructure is in a two-phase field with β-$Al_{12}Mg_{17}$, primarily preventing grain growth. Thus, once this intermetallic phase dissolves, rapid grain growth is

observed above 520 K. At higher temperatures, even the statistics on the azimuth are not representative anymore. However, some high-intensity regions, such as around azimuths of 113°, 235°, or 250°, fluctuate and show inclined timelines. These are fingerprints of grain reorientations, such as those studied recently by Liss et al. [19], which may lead to abnormal grain growth.

Figure 6c displays the profile of the azimuthal distribution at selected temperatures, showing the evolution from smooth rings to increasingly spiky and coarse distributions of the ultrafine-grained AZ31 alloy. The reflections of recrystallized grains, as well as in the mottled regime, are intrinsically sharp. The measure amounts between 0.13° and 0.16°, values which are given by the resolution of the binning, namely 0.125°, revealing more perfect crystallites with significantly reduced amounts of distortions caused by such as dislocations and subgrains. Note that there are discontinuities in the temporal behavior in Fig. 6, seen particularly in the zoomed areas (b), which we ascribe to a spontaneous displacement of the sample to the beam, as thermal expansion mismatch between the heating element ceramics and the specimen relaxes. Upon such an event, the beam spontaneously probes a different location in the microstructure.

Radial interpretation of reciprocal space: conventional powder diffractograms

Azimuthally integrated diffractograms of the Debye–Scherrer rings are presented in Fig. 7, illustrating color-mapped intensity against the modulus of the

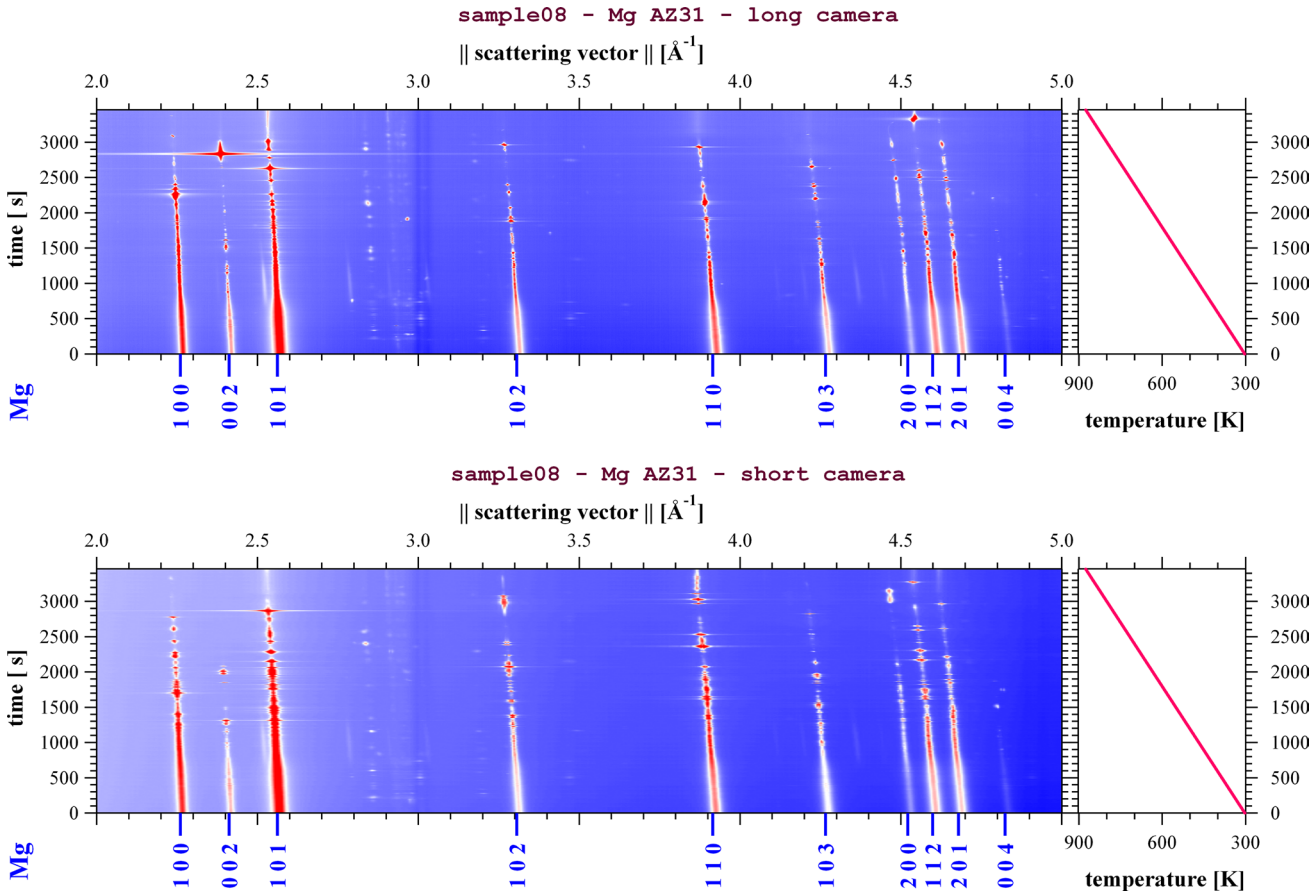

Figure 7 Azimuthally integrated diffractograms in upper and lower for the Debye–Scherrer ring with long and short camera lengths, respectively, as shown in Fig. 5, displaying the radial component, the modulus of scattering vector, against time on the left and the temperature profile on the right. The inclination of the lines is attributed to thermal expansion. Miller indices for the *hcp* Mg phase are shown. Notably, faint lines of a second phase become apparent between 614 and 1400 s (405–535 K), which has been determined to be β-$Al_{12}Mg_{17}$.

scattering vector and time. The upper and lower maps correspond to the Debye–Scherrer rings with long and short camera lengths, respectively, as shown in Fig. 5. The temporal evolution was recorded while subjecting the sample to a heat ramp, with the temperature scale provided to the right. One of the most striking features is the inclination of the lines toward shorter scattering vectors upon heating, which is the expression of thermal lattice expansion, which is discussed later. Second, some lines become interrupted due to grains growing so large that for some time, none of them fulfill the glancing condition for a given Laue–Bragg interference. Because of grain rotations and other fluctuations [19], the large, perfect grains reorient, cutting the Ewald sphere and reflecting spontaneously huge intensities. These strong reflections have intensities comparable to the incident beam, contributing air scattering as a background, resulting in the horizontal streaks in Fig. 7, e.g., at approximately 2830 s and 2865 s in the two detectors. Third, there is an apparent reduction of peak width beginning at around 614 s and 405 K, which we will investigate further. A closer look, best seen on Mg-112 and Mg-201, reveals that the thermal expansion is not linear with temperature. Furthermore, a second phase appears between 405 and 535 K in faint continuous lines just left of the Mg-101 peak and a few other locations. By reading these positions at 469 K and refining by hand matching an inner-centered cubic structure, we find a lattice parameter of $a = 10.577$ Å, which correlates with the β-$Al_{12}Mg_{17}$ intermetallic phase with space group $I\,\bar{4}\,3\,m$. Finally, there are some dots and spots emphasized between 2.8 and 3.0 $Å^{-1}$, which belong to larger particles of a different phase, probably a hard phase that has not been grain-refined during the high-pressure torsion process. As it is inert to the reaction processes, we disregard it further.

Peak widths and Williamson–Hall analysis

The breadths of the Gaussian fitted reflections of the long camera are displayed in Fig. 8a with their evolution in temperature for the high-pressure torsion-processed AZ31 alloy. Upon heating, first, they remain fairly constant, before a decrease sets in at about 350 K. The rate of decrease is largest between 405 and 427 K, then slowing down to saturation reached at 500 K. The change in peak width is evidence of microstructural changes with regimes of recovery before the width drop, recrystallization during the decrease in width, and some grain growth afterward [8, 11, 38]. At the higher temperatures, above said 427 K, the data fluctuate, which is due to the poor statistics from a relatively small number of large grains in the illuminated sample volume.

The Williamson–Hall plot is obtained when displaying the peak breadths against their scattering vector at selected temperatures of 300, 418, and 500 K, corresponding to the initial, intermediate, and last evaluated peak widths, as shown in Fig. 8b. Each trend line at these three temperatures in the plot reveals an ordinate intercept and a slope, which correlate with the reciprocal grain size and the microstrain gradient, respectively. As a function of heating time and thus temperature, the peak positions regarding the scattering vector vary by thermal expansion. These traces shown by rainbow color-graded vertical lines, representing each time step or temperature, are not straight but the S shape as seen in the zoomed Williamson–Hall plot of Fig. 8c, showing the peaks of Mg 112 and 201 reflections. Such regression for the peak width has been described for each time step of the S-shaped curves and is presented by intercept and slope in Fig. 8d, together with a representative example of the full width at half maximum of the Mg-100 reflection.

We estimate the resolution function to be approximately one order of magnitude smaller based on factors such as beam divergence through the aperture and lens distance. Other contributors, such as point spread at the detector, may have a similar impact. As a result, we will not consider instrument broadening in the subsequent discussion.

In the Williamson–Hall analysis, peak broadening results from two main factors: diffraction broadening due to the size of the small volume, represented by the coherent grain size D, which can be a subgrain or domain size, and strain gradient $\Delta\varepsilon$. It is worth noting that homogeneous strain only shifts a peak in response to changes in temperature or stress. Peak broadening, on the other hand, arises when variations in peak shifts caused by a strain gradient are integrated across the illuminated volume. Thus, we write for the variation of the reciprocal lattice vector G, i.e., the peak position,

$$\Delta G = K\frac{2\pi}{D} + \Delta\varepsilon G$$

where $K \approx 0.9$ is a shape factor, so to say, averaging over the thicknesses of a round particle. At $G = 0$, the

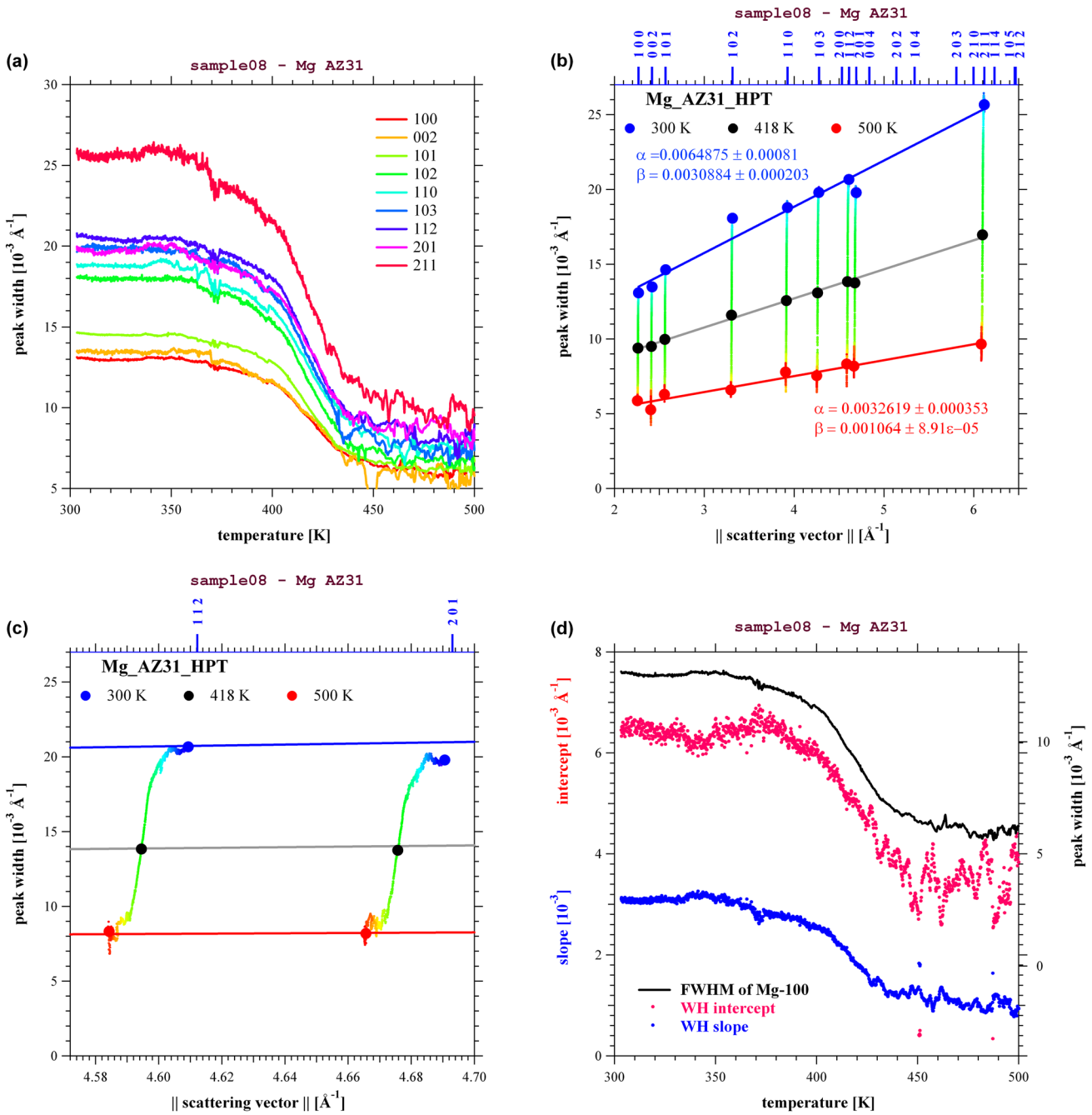

Figure 8 **a** Evolution of width for the Gaussian fitted reflections as temperature rises; **b** Williamson–Hall plot of widths against peak positions with emphasized points at 300 K, 418 K and 500 K, and fitted linear regressions; **c** zoomed region of the Williamson–Hall plot showing the evolution of the data in rainbow colors in (**b**), each color corresponding to the same time step or temperature; and **d** axis intercept and slope of the linear regression, evaluated for each measurement, against temperature, and width (FWHM) of the Mg-100 reflection, reproduced from (**a**).

intercept ΔG_0 allows the evaluation of the coherent grain size.

Here we obtain an initial intercept of $6.5 \cdot 10^{-3}$ Å^{-1} and thus a coherent grain size of 70 nm, which is a reasonable size as assumed earlier. In the literature, grain sizes of magnesium AZ31 after high-pressure torsion vary [14] and may depend minutely on processing temperature, heat dissipation in the anvil, and

aging. Masuda and Horita [39] report an average grain size of 150 nm; however, their transmission electron micrograph shows a high amount of structures on the 70 nm scale, which is consistent with our findings. We emphasize again that the Williamson–Hall evaluation shows the size of the coherent crystal volume, which can be the size of a subgrain structure, and thus is often smaller than grain sizes obtained by microscopy [40].

Evaluating the coherent grain size at 445 K, consistent with the temperature diffractograms displayed in Fig. 5, an intercept of $3.75{\cdot}10^{-3}$ Å^{-1} leading to 151 nm was computed from the Williamson–Hall plot. Such a value is surprisingly close to our evaluation in Fig. 5, measuring the spot distribution on the diffraction rings. Thus, this grain size obtained by two independent methods evaluates not only the procedures but also provides confidence in the results.

Upon further heating, the Williamson–Hall grain size seems to saturate at 200–300 nm, while the ring occupancy method estimates much larger sizes. As was stated, Williamson–Hall measures the coherent crystallite size, so to say the size of subgrains, while the ring occupancy method counts spots and a mosaic distribution—the latter being the orientation distribution of those subgrains. Therefore, the ring occupancy method represents the results close to the ones measured by microscopy, i.e., the overall grain size at which the grain can contain subgrains. Moreover, the Williamson–Hall method becomes inaccurate when grains approach a micrometer range, as then the reflection breadth becomes intrinsic. Therefore, the two methods of estimating the grain size transit seamlessly from the Williamson–Hall regime to the ring occupancy evaluation, using micrometer beam sizes.

The peak widths of all available Mg reflections at the examined temperatures displayed in Fig. 8b do not exactly lie on straight trend lines, which is called 'unsystematic' behavior. This apparent scatter is not given by the counting statistics but evolves smoothly as temperature increases. Therefore, it represents real strain anisotropy in the crystallites. Such strain anisotropy arises around dislocations, for which the *modified* Williamson–Hall method has been developed [41]. Its application to hexagonal systems, such as magnesium, is complex [42], as various kinds of slip systems exist, which are activated at different temperatures.

Qualitatively, it is evident that a highly unsystematic behavior of peak broadening is seen in the initial diffractograms of the high-pressure torsion-processed specimen at 300 K, attesting a high dislocation density in the severe plastically deformed material—similar to observations in *ccp* materials, e.g., CoCrFeNi [8, 43]. But, astonishingly, there exists an unsystematic behavior at 500 K, after the magnesium AZ31 has recrystallized and even had more time to recover. In addition, the unsystematic scatter of peak widths at 500 K (up, down, up, down, etc.) is qualitatively different from that at 300 K (down, down, up, up, etc.) as shown in Fig. 8d, which may be explained by dislocations sitting on different slip systems, as those are sequentially activated upon ramping the temperature. The rearrangement of slip systems during the temperature increase shows a striking consequence that the peak width distribution at 418 K lies on a straight line, meaning the structure is mostly dislocation-free upon recrystallization, while the dislocation density increases again upon further annealing.

A possible scenario regards the initial distortion with some recovery, the recrystallization at which the rate of decrease in peak width is maximal, followed by some grain growth. As recrystallization proceeds, highly distorted material is consumed to create new crystallites in the state of dislocation-free perfect crystals; therefore, the unsystematic scatter of peak width vanishes or becomes minimal, while the slope of the regression represents isotropic strain gradients due to stress or variation in composition. This minimal unsystematic behavior remains until 427 K that is shown in Fig. 8a, from where on it builds up continuously to the distribution seen at 500 K. At those 427 K, the grain interactions leading to their growth take over, containing torques between grains, leading to grain reorientation, which explains the obtained azimuth–time plots in Fig. 6a and b. Such grain rotations and fluctuations at higher temperatures are typical for magnesium and have been observed coincidentally [16–18], as well in a recent dedicated study on abnormal grain growth upon grain coalescence [19]. The latter discusses the need for high diffusive mass transport in order to accommodate the embedded shape of the crystallite upon rotation, according to the Harris [44] and Moldovan [45] models. Therein mass transport is entirely explained by predominant grain boundary diffusion, which is based on the Raj–Ashby linear model [46] describing the Lifshitz regime of grain boundary sliding under low stresses [47, 48]. As grains grow, diffusion paths around all of a given grain become too large while torque tractions applied by different neighbors compete, such that dislocations

are expulsed into the bulk of the grain, comparable to the regime of Rachinger sliding [48, 49]. This scenario of high-temperature induced dislocations even after long annealing is supported by the fact that the final unsystematic scatter at 500 K of the annealed high-pressure torsion-processed material resembles well to those observed by neutron diffraction on the as-received material (Fig. 4b). Moreover, the neutron data show strain homogenization upon holding at 700 K, while the unsystematic scatter prevails, and thus, the dislocations involved. The unsystematic scatter of the as-received specimen does not change its character, in contrast to the severe plastically deformed material, revealing that the as-received material contains already a lot of the high-temperature induced dislocations, while the nanostructured material is overwhelmed by the plastic grain refinement and thus the action of the twinning and slip systems which were activated at room temperature. It is well known that the dislocation structures in plastically deformed magnesium systems depend strongly on the processing temperature [50]. In the as-received material, the character of unsystematic scatter barely evolves. However, in the case of high-pressure torsion-processed magnesium, it undergoes significant changes in its characteristics, leading to the conclusion that the as-received sheet was likely manufactured through warm rolling, well above the $Al_{12}Mg_{17}$ dissolution temperature of 486 K, where high-temperature slip systems were already activated. On the other hand, the nanostructured material has been severely deformed at room temperature, resulting in the exposure of fewer slip systems but a noticeable presence of twinning, resulting in the observed unsystematic scatter initial to the heating experiment.

To resume this chapter, we have identified three regimes of thermal evolution namely annealing recovery peaking at 350 K, followed by the onset and full recrystallization between 405 and 427 K, and subsequently, sluggish grain growth in a two-phase field. Initially existing dislocations are removed during recrystallization, at which the crystallites are mostly dislocation-free; however, new dislocations on newly activated slip systems build up due to fluctuating grain rotations at higher temperatures.

Lattice expansion and anomalies

Thermal-induced lattice expansion has been revealed from the peak positions of all observed Mg reflections with respect to 300 K and is displayed in Fig. 9a. At lower temperatures between 303 and 320 K that are given by the first 100 data points in the experiment, they all superimpose within their point scatter and behave linearly. Their slopes are the thermal expansion coefficients for each reflection plane, plotted in Fig. 9b against their square of direction sines with respect to the scattering vector to the crystallographic c axis. In principle, the thermal expansion coefficient α_{ij} is a second-rank tensor, relating temperature to thermal strain. The symmetry of a hexagonal system allows for two independent components α_c and α_a, parallel and perpendicular to the c axis, respectively [51]. This would lead to a strain ellipsoid, or a straight line in a plot of thermal expansion against the square of the direction sines of orientation angle ψ with respect to c. The data plotted in Fig. 9b, however, do not show such systematic anisotropy. They scatter around the mean value. Thus, thermal expansion is isotropic with a coefficient of $\alpha_c = \alpha_a = 24.63 \cdot 10^{-6}\ K^{-1}$ for the high-pressure torsion-processed AZ31.

As already stated, thermal expansion has been found almost isotropic in Mg since the early years [29]. The value of thermal expansion for the high-pressure torsion-processed AZ31 is significantly lower than measured for the initial as-rolled sheet material measured by neutron scattering in the present study as well as by Liu et al. [16], even a little lower than the reported values by Childs [29]. The thermal expansion coefficient of magnesium alloys is ranging typically from $26 \cdot 10^{-6}\ K^{-1}$ to $32 \cdot 10^{-6}\ K^{-1}$ [31], depending on composition and microstructure. In many situations, including other metals, the best values for measuring the thermal expansion coefficient are measured upon cooling from the recovered high-temperature microstructure. e.g., on Al-10Sr [25], CoCrFeNi high-entropy alloy [8], and stainless steel [38]. In the present situation, however, we do not have any cooling data, which would neither make sense due to the large grown grain size and a microbeam diffraction setup.

Figure 9c presents the difference between the total measured lattice strain and the linear extrapolated low-temperature thermal expansion, clearly showing a positive strain bump for each lattice plane family. Fitted Gaussians are drawn to the bell-shaped data between 300 and 500 K for the evaluated reflections.

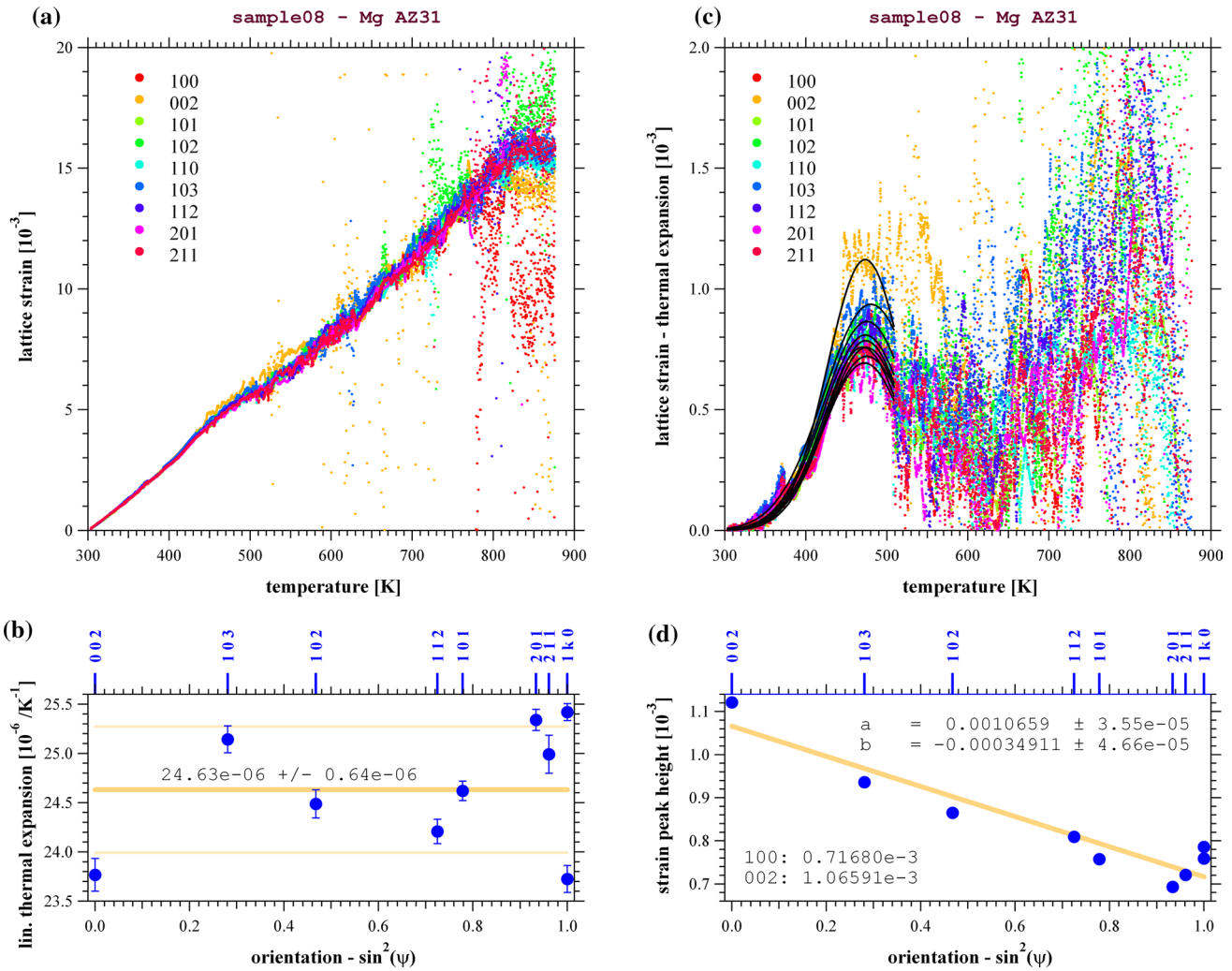

Figure 9 **a** Total lattice strain as a function of temperature of the high-pressure torsion-processed specimen, evaluated from the positions of the fitted peaks recorded by the long camera. The scatter at high temperature is when fitting failed. **b** Linear thermal expansion coefficients for the analyzed reflections as fitted to the total lattice strain in **a** at the lower temperatures, plotted against square of sine of orientation angle ψ of the scattering vectors to the crystallographic *c* axis. The thick and thin yellow lines are average and ± standard deviation. **c** Nonlinear part of lattice strain, i.e., the difference of total strain and aforementioned linearized thermal expansion values, revealing a strain bump, to which Gaussians have been fitted between 300 and 500 K. **d** Amplitudes of the Gaussians as a function of orientation angle ψ with a linear fit to the coordinates.

Careful analysis reveals that deviations from the linear change in thermal expansion develop as low as 342 K, leading to a strain bump with a maximum at around 472 K. Above that range, fluctuations become too large, but one can see a decrease in this additional strain component back to the original, linearized thermal expansion, keeping in mind that the coefficient slightly increases monotonically with temperature. The amplitudes of the strain bump are plotted in Fig. 9d against lattice plane orientation, demonstrating indeed an anisotropic behavior parallel and perpendicular to the crystallographic *c* axis, as allowed by crystal symmetry for this 2nd rank strain tensor. With values of $\Delta\varepsilon_c = 1.07 \cdot 10^{-3}$ and $\Delta\varepsilon_\alpha = 0.72 \cdot 10^{-3}$ along and perpendicular to *c*, respectively, the anisotropy of this strain bump amplitude is significant and scales by a factor of 1.49. The volume-averaged linear strain amplitudes compute to $(\Delta\varepsilon_c + 2\,\Delta\varepsilon_\alpha)/3 = 0.83 \cdot 10^{-3}$.

The strain bump goes along with the phase transformation of β-$Al_{12}Mg_{17}$, as already shown in Fig. 7. The intensity of the superimposed β-552 and β-721 peaks, located around 4.36 $Å^{-1}$ that is visible especially in the

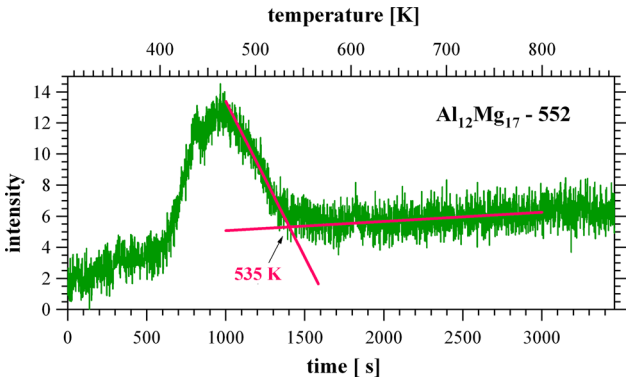

Figure 10 Intensity evolution of the superimposed β-552 and β-721 Laue–Bragg interferences of the $Al_{12}Mg_{17}$ phase as a function of time and temperature, appearing at 405 K and ceasing at 535 K.

lower plot of Fig. 7, is presented against the time of heating and thus temperature in Fig. 10. It appears at 405 K and ceases mainly at 535 K, while its maximum prevail coincides with the strain bump maximum at 472 K as shown in Fig. 9b. It is well known that smaller Al atoms in solid solution in a Mg matrix exert a chemical strain of approximately $-1.15{\cdot}10^{-3}$ per atomic percent of aluminum [52], playing a pivotal role in Mg ↔ $Al_{12}Mg_{17}$ phase transformations [16]. Indeed, Murray reports on the anisotropy of this chemical strain [52]. The slopes in her plots are evaluated into $1.14686{\cdot}10^{-3}$ and $0.99938{\cdot}10^{-3}$ per at.% Al in Mg for the *c* and *a* directions, respectively. Their orientation averaged linear slopes, $(\delta\varepsilon_c + 2\delta\varepsilon_a)/3$, computes to $1.05{\cdot}10^{-3}$ per at.% Al or $0.94{\cdot}10^{-3}$ per mass-% Al, and the ratio is $\delta\varepsilon_c/\delta\varepsilon_a = 1.14757 = 0.871405^{-1}$. Comparing this to our results on the strain bump amplitude, we obtain a present ratio of 1.49 larger along *c* than along *a* which is significantly greater than Murray's ratio of 1.14757. In other words, 77% of the strain bumps are accounted for the depletion of Al in the Mg matrix, while 23% are so far unaccounted for, based on the asymmetry measurements.

The phase fraction of β-$Al_{12}Mg_{17}$ can be estimated by comparing the diffraction peak intensities of the Mg-101 and the β-330 Laue–Bragg interferences, which lie very close to each other around 2.52 $Å^{-1}$ (see upper plot of Fig. 7) and evaluated to $I_\beta/I_{Mg} = 9.3336{\cdot}10^{-3}$. Using the powder diffraction program CrystalDiffract®, we simulate the theoretical intensity ratio for a 1:1 volume fraction to obtain an expression for the β volume fraction being $f_{V,\beta} = I_\beta/I_{Mg} * 0.890$. The densities are $\rho_\beta = 2.05$ g/cm^3 and $\rho_{Mg} = 1.738$ g/cm^3 for the intermetallic and Mg, respectively, giving a mass fraction $f_{m,\beta} = f_{V,\beta}\ \rho_\beta/\rho_{Mg}$. We obtain $f_{V,\beta} = 8.31{\cdot}10^{-3}$ and a β-$Al_{12}Mg_{17}$ mass fraction of $f_{m,\beta} = 9.80{\cdot}10^{-3}$.

The mass fraction of Al in stoichiometric $Al_{12}Mg_{17}$ is 44%, meaning precipitating β-phase having $f_{m,\beta} = 9.80{\cdot}10^{-3}$ results in a change of − 0.43% of Al mass in the Mg solid solution. This would lead to an average chemical strain of $+0.41{\cdot}10^{-3}$. Thus, the chemical strain due to the phase transformation accounts for only about half of the observed strain bump with an amplitude of $0.83{\cdot}10^{-3}$. An excess strain amplitude of $\delta\varepsilon_v = 0.42{\cdot}10^{-3}$ is still unaccounted for the observed strain bump.

Consideration of both phase precipitation and strain anisotropy independently estimates a significantly smaller amplitude of strain changes than observed in the experiment. Therefore, another mechanism than the depletion of Al atoms from the supersaturated solid solution needs to be examined. In the past, Liu et al. [8] reported on strain anomalies during the recrystallization process in a high-pressure torsion-processed CoCrFeNi high-entropy alloy, which were accommodated by a high concentration of excess vacancies. A similar strain deficit was observed on likewise treated stainless steel [38]. With this, we conclude on three contributions to make up the total strain, namely thermal expansion due to the anharmonicity of the atomic binding potential, chemical strain due to segregation of Al atoms, and vacancy strain due to the volume relaxation of the crystal lattice around a vacancy.

In this regard, a further lattice expansion anomaly can be observed at 827 K as shown in Fig. 9a and c, coinciding with trespassing the solidus of AZ31 alloy [53], at which partial melting starts. Generally, the thermal expansion coefficients of pure magnesium vary with temperature. Above 500 K, they become continuously larger than the values at room temperature, particularly above 700 K [29]. A similar tendency is observed also for the nanostructured AZ31 as shown in Fig. 9b where, despite the bad statistics, an augmenting trend is observed. Although atomic interaction potentials may play a major role, some of this augmented expansion must be attributed to our vacancy expansion model, due to the thermal activation of vacancies. At 827 K, we observe in Fig. 9a that lattice strain stagnates upon further heating. This is the regime of gradual melting, at which, according

to the quasibinary phase diagram [53], Al depletes in the Mg matrix—which would lead to a stronger positive strain. However, we ignore the kinetics and possible segregation of the Zn component, which may lead to a stagnating effect.

Vacancy formation upon recrystallization

In order to account for the yet unexplained excess strain bump of $\delta\varepsilon_v = 0.42 \cdot 10^{-3}$, we consider lattice widening by a large amount of vacancies. Let us set for the relative change of total volume, $\Delta V/V = (2\delta\varepsilon_a + \delta\varepsilon_c) = 3\,\delta\varepsilon_v = c_{\mathrm{eff}}\,\delta\Omega/\Omega$, where c_{eff} is the number concentration of effective atomic volumes affected by vacancy strain, Ω is the atomic volume and $\delta\Omega$ is the relaxation volume around a vacancy. Thus, $c_{\mathrm{eff}} = \Delta V/V * \Omega/\delta\Omega$. With a conservative relaxation volume, say $\delta\Omega/\Omega = -0.13$ [54], we obtain $c_{\mathrm{eff}} = 9.7 \cdot 10^{-3}$. As in Liu's paper [8] we assume, the average local strain of $\delta\Omega/\Omega$ spreads over two atom shells around each vacancy to each dimension, supported by Sahoo et al. [55] reporting a spread over 'two spheres,' affecting 64 atoms, the vacancy concentration is $c_v = c_{\mathrm{eff}}/64 = 1.5 \cdot 10^{-4}$.

Such vacancy concentration is extremely high, surpassing those at melt. Chetty et al. [56] reported the activation energy for vacancy formation in Mg to be 0.835 eV which would lead to a vacancy concentration of $0.3 \cdot 10^{-4}$ at 923 K—a factor of five smaller than our value during recrystallization.

The vacancy concentrations we estimate by simple models are an order of magnitude higher than thermally activated at melting temperature. A similar trend has been found in our CoCrFeNi work [8]. It is, however, estimated within the range of vacancy concentrations at melting as the reported activation energy spreads quite a bit in the literature. Chetty [56] cites other papers with activation energies for vacancy formation being 0.81, 0.58, 0.78, 0.90 eV, which results in thermal activated vacancy concentrations of $[0.38, 6.81, 0.55, 0.12] \cdot 10^{-4}$.

The offset between heating and cooling in CoCrFeNi [8] as well as in stainless steel [38] has been attributed to high excess vacancy concentrations created by high-pressure torsion. Such concentrations of 10^{-4} to 10^{-3} are well supported by positron annihilation spectroscopy on various metals, which are created during the processing at room temperature [57]. Moreover, Ungár et al. [58] measured vacancy concentrations by the increase in the diffuse synchrotron X-ray scattering during plastic deformation and also reported a shift of Bragg peaks due to vacancies. However, a quantitative evaluation has been introduced only by Liu et al. [8] and in the present work. In addition to those excess vacancies caused by severe plastic processing, here we observe the creation of vacancies during the recrystallization process, leading to a peak of vacancies that then vanishes again at higher temperatures due to thermalization.

The big picture of thermal evolution in nanostructured magnesium alloy

The in situ heating experiment on high-pressure torsion-processed magnesium AZ31 alloy by microbeam high-energy X-ray diffraction reveals multidimensional insights into the evolution of the microstructure and its kinetics. In particular, the azimuthal investigation of the morphology of intensity distribution determines regimes of recovery up to 405 K, recrystallization until 427 K, sluggish two-phase grain growth and rearrangements, i.e., grain reorientation, up to 520 K, followed by rapid and large and erratic grain growth in a single-phase filed. These azimuthal observations go hand in hand with radial peak shifts, anomalies in thermal expansion, the reduction of peak broadening, and the precipitation and dissolution of β-$Al_{12}Mg_{17}$ phase. Apart from fairly constant thermal expansion and a little recovery until 550 K, none of the abovementioned effects take place under heating in the as-received rolled sheet material.

The first stunning difference of the high-pressure torsion-processed specimen from the as-received sheet is the precipitation of β-$Al_{12}Mg_{17}$ phase appearing at 405 K and dissolving at 535 K in the nanostructured, while it lacks in the as-received material. Regarding the phase diagram [53], it should exist in equilibrium below 486 K and then dissolve in the matrix. We can realistically assume that the material has been quenched from the single-phase field during its production, so that we start with a single supersaturated *hcp* Mg phase. Upon heating, diffusion sets in, driving to the thermodynamic equilibrium. However, the diffusivity of Al in Mg is only about 10^{-18} m^2/s around 500 K, resulting in diffusion lengths of 50 nm over the time of heating of maximal optimistic 800 s at the range of interest. This is by orders of magnitude smaller than the ~ 10 μm grain size of the as-received sheet. Since most nucleation sites occur at

grain boundaries, necessary diffusion lengths are not met, and therefore, the sheet material does not show any phase transformation or related lattice parameter anomaly in the neutron scattering experiment. We can argue now, grain sizes and nucleation center distributions of the nanostructured material match the calculated diffusion length of 50 nm, but that would mean, during the experiment we would have only a small amount precipitated and dissolved again. However, the β-$Al_{12}Mg_{17}$ phase pops up and evolves rapidly at 405 K. This necessitates much enhanced diffusion. Hence, the excess vacancies can help, with concentrations overpassing those at the melting point, increasing diffusivities beyond those at the melting point. The latter range about 10^{-12} m^2/s [59] leading to a diffusion length of conservative 2 μm per 1 s of detector exposure time, which is now much larger than the grain size of the ultrafine-grained material. Thus, phase transformation can take place.

The scenario of the enhanced diffusion during recrystallization is the following: Due to the high distortion of the nanostructured material containing ample of dislocations and intergranular stresses, as evidenced by the Williamson–Hall plot in Fig. 8b, the driving force is high for recrystallization, which is most violent between 405 and 427 K. Such a process needs a lot of mass transport, driven by the stored energy and enabled through diffusion. Basically, the entire recrystallized volume has moved its atoms. This implements the driving force is high enough to stimulate diffusion, i.e., to create excess vacancies propagating the diffusion process in a close-packed crystal structure. As a side effect, the equilibrium phase of β-$Al_{12}Mg_{17}$ is led to precipitate. Indeed, the steepest and linear raise of intensity for the β-$Al_{12}Mg_{17}$ precipitate in Fig. 10 lies exactly in the range of recrystallization between 404 and 427 K. After this, the precipitation saturates to equilibrium and eventually ceases by the phase diagram upon further heating, with a transformation–temperature–time-delay. Moreover, during recrystallization, the Williamson–Hall plot in Fig. 8b shows a straight-line 'systematic' behavior and the azimuthal widths of single-grain reflection spots in Fig. 6c, i.e., the mosaic spread of the new crystallites, are intrinsic, esteeming crystallites with significantly reduced dislocation densities. With the findings of a recent paper [19], we can expect that the recrystallization of grains and their boundaries are highly activated underlined by the high diffusivity, eating up the sluggishly evolving non-recrystallized material. Recrystallization vacancies are formed upon the recrystallization process, which specifically is after nucleation and during the growth of a recrystallized grain. Such recrystallization vacancies would then be found in the recrystallized volume, while we predict lower concentrations prevailing in the non-recrystallized regions, as that material has not yet released its stored energy to create the additional excess vacancies. The high concentration of recrystallization vacancies is an express channel for enhanced diffusion driving the kinetics of the reordering process. The highly activated volumes, especially their highly activated grain boundaries at their forefront, keep the process up until all material has been recrystallized.

A second striking feature is the anisotropy of lattice expansion due to point defects. While thermal expansion is incidentally isotropic, chemical strain due to Al substitutional point defects as well as strain due to vacancies is anisotropic, as much as it is allowed by the symmetry of the hexagonal space group. As was mentioned earlier, Murray indirectly reports a chemical strain anisotropy of $\delta\varepsilon_c/\delta\varepsilon_a = 1.14757$ upon substituting Al on the Mg lattice. We measure a strain anisotropy ratio for the ultrafine-grained Mg AZ31 of 1.49, which partly evolves by Al substitution and partly by vacancies. This means the anisotropy effect in strain is larger upon vacancies than on Al substitutes. Both Al substitutes and vacancies are point defects, and both reduce the local volume at their site. The Al atom is 0.83 times smaller than the Mg atom while the vacancy is intrinsically smaller. It seems the anisotropy in strain scales with the 'size' of the point defect. Moreover, shorter jump distances mean higher diffusivities. Thus, the crystal direction of a smaller vacancy strain should match a larger diffusivity, which has indeed been observed by Shewmon, reporting larger diffusivity perpendicular to c than parallel to c [30].

Epilogue and future prospective

The significant findings of the current in situ diffraction study on high-pressure torsion-processed magnesium alloy AZ31 pertain to the kinetics involved in the recrystallization process, transitioning from a highly distorted nanostructure to more perfect crystallites. An expedited phase transformation resulting in the precipitation of intermetallic compound $Al_{12}Mg_{17}$ from the supersaturated Mg phase has been observed. This is in contrast to heating the as-received material.

The overall observed lattice strain comprises regular thermal expansion due to the anharmonicity of the atomic binding potential, chemical strain due to the segregation of Al from the matrix, and an expansion attributed to the presence of high concentrations of athermal vacancies. These vacancies are generated during processing, maintained due to the high stored energy in the nanostructured material, and can even surpass vacancy concentrations as high as those seen at the melting point. Virtually every atom needs to be moved during the recrystallization process, necessitating large diffusivities. These diffusivities are much greater than what would be expected based on the usual Arrhenius law for thermally activated processes. In close-packed materials like *hcp* magnesium, diffusion is facilitated by vacancies, leading to a correlation between high vacancy concentrations and high diffusivity.

However, these mechanisms during recrystallization have not been directly investigated, as measuring them in situ during the relatively short timescales of recrystallization can be challenging. There is a need to quantify these mechanisms during the recrystallization process, which may inspire ideas for future experimental investigations. Some of the states, such as vacancy concentrations, may be quenched, but diffusivities have to be measured in real time on the fly.

A complementary measurement of recrystallization vacancies can be explored using positron lifetime spectroscopy [57, 60]. In this method, positrons (positive antimatter electrons) become trapped within vacancies and eventually annihilate with an electron, emitting gamma radiation. As the electron density within the vacancy decreases, the positron lifetime is extended, as opposed to interstitial trapping. The signal height in this method is directly related to the vacancy concentration.

Self-diffusivities in metals at high temperatures have traditionally been studied using techniques such as quasielastic neutron scattering [61, 62] and quasielastic Mößbauer spectroscopy [62, 63]. Advanced variations of X-ray Mößbauer spectroscopy involve the use of synchrotron radiation [64]. These nuclear methods not only provide information about jump frequencies during the diffusion process but also measure the jump vector by analyzing the self-correlation function of atoms during the jump. However, these methods have limitations, as they are applicable to only certain types of atoms with appropriate scattering cross sections.

The neutron method, for instance, relies on the incoherent part of scattering, which can be substantial for specific isotopes within the material under investigation. Mößbauer and nuclear resonant spectroscopy are primarily limited to compounds containing iron due to its nuclear resonance properties of the ^{57}Fe isotope. Additionally, these techniques are typically limited to high temperatures where diffusion rates are relatively fast.

Nonetheless, during recrystallization, we anticipate very high diffusivities, and the restricted selection of elements is sufficient for a range of sample systems in our studies. For example, iron-containing compounds have been part of our research, including the previously studied CoCrFeNi high-entropy alloy [8] and stainless steel [38]. Additionally, aluminum-containing systems are accessible by the neutron technique, allowing us to investigate Al–Mg compositions, such as supersaturated, mechanically alloyed metals [6].

Performing recrystallization measurements using inelastic nuclear methods can be quite challenging due to the limited times available during recrystallization. Special experimental setups are needed to address this issue. For instance, one approach involves continuously shifting a long, severely plastically deformed specimen through a temperature gradient. This setup ensures that recrystallization occurs at the optimal rate within the specific region of interest within the gauge volume of the spectrometer.

Overall, there is a significant need for intriguing experimental work to be carried out in order to provide in situ clarification of the atomic diffusion and vacancy mechanisms during the recrystallization process. Other open research themes are the indicated creation of dislocations at high temperature upon grain coalescence, which is counterintuitive to the annealing effect, as well as the mechanisms of steady-state plastic deformation processes in a wider sense. Moreover, theoretical and computer-supported modeling needs to be undertaken to further validate such groundbreaking experiments.

Acknowledgements

This study was supported in part by the National Science Foundation of the United States under Grant No. CMMI-2051205. The authors greatly acknowledge

neutron beam time and support at the Materials and Life Science Experimental Facility (MLF) at the Japan Proton Accelerator Research Complex (J-PARC), Japan, using the Takumi diffractometer at beamline 19 beneath the user program proposal number 2014A0267. Synchrotron beam time is greatly acknowledged at the beamline P21.2 at PETRA-III at the Deutsches Elektronen-Synchrotron DESY, Germany, under user proposal number I-20200639.

Funding

Open Access funding enabled and organized by CAUL and its Member Institutions.

Data availability

The datasets generated during the experiments and analyzed under the current study are available from the corresponding authors upon reasonable request.

Declarations

Conflict of interest The authors declare no conflict of interest.

Ethical approval The authors have adhered to the accepted ethical standards of a genuine research study.

Open Access This article is licensed under a Creative Commons Attribution 4.0 International License, which permits use, sharing, adaptation, distribution and reproduction in any medium or format, as long as you give appropriate credit to the original author(s) and the source, provide a link to the Creative Commons licence, and indicate if changes were made. The images or other third party material in this article are included in the article's Creative Commons licence, unless indicated otherwise in a credit line to the material. If material is not included in the article's Creative Commons licence and your intended use is not permitted by statutory regulation or exceeds the permitted use, you will need to obtain permission directly from the copyright holder. To view a copy of this licence, visit http://creativecommons.org/licenses/by/4.0/.

References

[1] Gubicza J (2020) Annealing-induced hardening in ultrafine-grained and nanocrystalline materials. Adv Eng Mater 22:1900507. https://doi.org/10.1002/adem.201900507

[2] Liss K-D, Bartels A, Schreyer A, Clemens H (2003) High-energy X-rays: a tool for advanced bulk investigations in materials science and physics. Textures Microstruct 35:219–252. https://doi.org/10.1080/07303300310001634952

[3] Liss KD (2023) In-situ neutron and synchrotron methods for the investigation of plastic deformation and annealing in metals. Mater Res Proc 32:25–40. https://doi.org/10.21741/9781644902615-3

[4] Han J-K, Liss K-D, Langdon TG, Kawasaki M (2019) Synthesis of a bulk nanostructured metastable Al alloy with extreme supersaturation of Mg. Sci Rep 9:17186. https://doi.org/10.1038/s41598-019-53614-3

[5] Han J-K, Liss K-D, Langdon TG et al (2020) Mechanical properties and structural stability of a bulk nanostructured metastable aluminum-magnesium system. Mater Sci Eng A 796:140050. https://doi.org/10.1016/j.msea.2020.140050

[6] Han J-K, Sugimoto K, Kawasaki M, Liss K-D (2022) Strain-dependent phase transformation mapping of diffusion-bonded nanocrystalline aluminum-magnesium by high-energy synchrotron X-rays. Mater Lett 321:132414. https://doi.org/10.1016/j.matlet.2022.132414

[7] Paul A, Liu X, Kawasaki M, Liss K-D (2023) Inverted magnetic response in severe plastically deformed nanostructured high-entropy alloy. Appl Phys Lett 122:052402. https://doi.org/10.1063/5.0138040

[8] Liu X, Han J-K, Onuki Y et al (2023) In situ neutron diffraction investigating microstructure and texture evolution upon heating of nanostructured CoCrFeNi high-entropy alloy. Adv Eng Mater 25:2201256. https://doi.org/10.1002/adem.202201256

[9] Schuh B, Mendez-Martin F, Völker B et al (2015) Mechanical properties, microstructure and thermal stability of a nanocrystalline CoCrFeMnNi high-entropy alloy after severe plastic deformation. Acta Mater 96:258–268. https://doi.org/10.1016/j.actamat.2015.06.025

[10] Kawasaki M, Han J-K, Liu X et al (2023) Synchrotron high-energy X-ray & neutron diffraction, and laser-scanning confocal microscopy: *In-Situ* characterization techniques for bulk nanocrystalline metals. Mater Trans 64:1683–1694. https://doi.org/10.2320/matertrans.MT-MF2022022

[11] Kawasaki M, Han J-K, Moon S-C, Liss K-D (2023) In-situ heating observations on microstructure relaxation of ultrafine-grained high-entropy alloys using neutron diffraction and laser-scanning confocal microscopy. Mater Res

Proc. 32:235–243. https://doi.org/10.21741/9781644902615-27

[12] Kamrani S, Fleck C (2019) Biodegradable magnesium alloys as temporary orthopaedic implants: a review. Biometals 32:185–193. https://doi.org/10.1007/s10534-019-00170-y

[13] Zhao D, Witte F, Lu F et al (2017) Current status on clinical applications of magnesium-based orthopaedic implants: a review from clinical translational perspective. Biomaterials 112:287–302. https://doi.org/10.1016/j.biomaterials.2016.10.017

[14] Figueiredo RB, Langdon TG (2019) Processing magnesium and Its alloys by high-pressure torsion: an overview. Adv Eng Mater 21:1801039. https://doi.org/10.1002/adem.201801039

[15] Miyamoto H (2016) Corrosion of ultrafine grained materials by severe plastic deformation, an overview. Mater Trans 57:559–572. https://doi.org/10.2320/matertrans.M2015452

[16] Liu X, Xu P, Shiro A et al (2022) Heat-induced structural changes in magnesium alloys AZ91 and AZ31 investigated by in situ synchrotron high-energy X-ray diffraction. J Mater Sci 57:21446–21459. https://doi.org/10.1007/s10853-022-07917-y

[17] Liss K-D, Yan K, Reid M (2014) Physical thermo-mechanical simulation of magnesium: an in-situ diffraction study. Mater Sci Eng A 601:78–85. https://doi.org/10.1016/j.msea.2014.02.014

[18] Liss K-D (2017) Structural evolution of metals at high temperature: complementary investigations with neutron and synchrotron quantum beams. In: Solanki KN, Orlov D, Singh A, Neelameggham NR (eds) Magnesium technology 2017. Springer International Publishing, pp 633–638

[19] Liss K-D, Xu P, Shiro A et al (2023) Abnormal grain growth: a spontaneous activation of competing grain rotation. Adv Eng Mater 2300470. https://doi.org/10.1002/adem.202300470

[20] Liss K-D, Yan K (2010) Thermo-mechanical processing in a synchrotron beam. Mater Sci Eng: A 528(1):11–27. https://doi.org/10.1016/j.msea.2010.06.017

[21] Harjo S, Ito T, Aizawa K et al (2011) Current status of engineering materials diffractometer at J-PARC. Mater Sci Forum 681:443–448. https://doi.org/10.4028/www.scientific.net/MSF.681.443

[22] Nakajima K, Kawakita Y, Itoh S et al (2017) Materials and life science experimental facility (MLF) at the Japan proton accelerator research complex II: neutron scattering instruments. Quantum Beam Sci 1:9. https://doi.org/10.3390/qubs1030009

[23] Liss K-D (2018) Materials and life science with quantum beams at the Japan proton accelerator research complex. Quantum Beam Sci 2:9. https://doi.org/10.3390/qubs2020010

[24] Machiya S, Osamura K, Hishinuma Y, Taniguchi H, Harjo S, Kasawaki T (2023) Measurement of mechanical behavior of ^{11}B enriched MgB_2 wire using pulsed neutron source. Quantum Beam Sci 7:34. https://doi.org/10.3390/qubs704003

[25] Liss K-D, Harjo S, Kawasaki T et al (2021) Anisotropic thermal lattice expansion and crystallographic structure of strontium aluminide within Al-10Sr alloy as measured by in-situ neutron diffraction. J Alloys Compd 869:159232. https://doi.org/10.1016/j.jallcom.2021.159232

[26] Lienert U, Gutschmidt S, Zimmermann VM et al (2013) Beamline P21: Swedish high energy materials science beamline. Deutsches Elektronen Synchrotron (DESY), Hamburg

[27] Böhm J, Wanner A, Kampmann R et al (2003) Internal stress measurements by high-energy synchrotron X-ray diffraction at increased specimen-detector distance. Nucl Instrum Methods Phys Res Sect B-Beam Interact Mater At 200:315–322. https://doi.org/10.1016/S0168-583X(02)01694-4

[28] Kollenberg W, Margalit J (1992) Thermal expansion of AlON and γ-Al2O3. J Mater Sci Lett 11:991–993. https://doi.org/10.1007/BF00729903

[29] Childs BG (1953) The thermal expansion of anisotropic metals. Rev Mod Phys 25:665–670. https://doi.org/10.1103/RevModPhys.25.665

[30] Shewmon PG (1956) Self-diffusion in magnesium single crystals. JOM 8:918–922. https://doi.org/10.1007/BF03377790

[31] Cverna F (2002) Chapter 2: thermal expansion. In: ASM ready reference - thermal properties of metals. ASM International, Materials Park, Ohio 44073-0002

[32] Harjo S, Gong W, Kawasaki T (2023) Stress evaluation method by neutron diffraction for HCP-structured magnesium alloy. Quantum Beam Sci 7:32. https://doi.org/10.3390/qubs7040032

[33] Komatsuzaki K, Yukutake E (2005) Research on microstructure refinement and processing characteristics of magnesium alloys. Ibaraki Prefectural Industrial Technology Center, Ibaraki Prefecture. https://www.itic.pref.ibaraki.jp/publication/research_h17/

[34] Malheiros LRC, Figueiredo RB, Langdon TG (2015) Grain size and microhardness evolution during annealing of a magnesium alloy processed by high-pressure torsion. J Mater Res Technol 4:14–17. https://doi.org/10.1016/j.jmrt.2014.10.008

[35] Lee H-J, Lee SK, Jung KH et al (2015) Evolution in hardness and texture of a ZK60A magnesium alloy processed by

high-pressure torsion. Mater Sci Eng A 630:90–98. https://doi.org/10.1016/j.msea.2015.02.011

[36] Yan K, Liss K-D, Garbe U et al (2009) From Single Grains to Texture. Adv Eng Mater 11:771–773. https://doi.org/10.1002/adem.200900163

[37] Liss K-D, Garbe U, Li H et al (2009) In situ observation of dynamic recrystallization in the bulk of zirconium alloy. Adv Eng Mater 11:637–640. https://doi.org/10.1002/adem.200900094

[38] Kawasaki M, Han J-K, Liu X et al (2022) In situ heating neutron and X-ray diffraction analyses for revealing structural evolution during postprinting treatments of additive-manufactured 316L stainless steel. Adv Eng Mater 24:2100968. https://doi.org/10.1002/adem.202100968

[39] Masuda T, Horita Z (2019) Grain refinement of AZ31 and AZ61 Mg alloys through room temperature processing by UP-scaled high-pressure torsion. Mater Trans 60:1104–1110. https://doi.org/10.2320/matertrans.M2018308

[40] Kerber MB, Zehetbauer MJ, Schafler E et al (2011) X-ray line profile analysis—an ideal tool to quantify structural parameters of nanomaterials. JOM 63:61–70. https://doi.org/10.1007/s11837-011-0115-1

[41] Ungár T, Gubicza J (2002) Grain Size, size-distribution and dislocation structure from diffraction peak profile analysis. In: Ultrafine grained materials II. John Wiley & Sons, Ltd, pp 595–604

[42] Klimanek P, Kužel R (1988) X-ray diffraction line broadening due to dislocations in non-cubic materials. I. General considerations and the case of elastic isotropy applied to hexagonal crystals. J Appl Crystallogr 21:59–66. https://doi.org/10.1107/S0021889887009580

[43] Zhao W, Han J-K, Kuzminova YO et al (2021) Significance of grain refinement on micro-mechanical properties and structures of additively-manufactured CoCrFeNi high-entropy alloy. Mater Sci Eng A 807:140898. https://doi.org/10.1016/j.msea.2021.140898

[44] Harris KE, Singh VV, King AH (1998) Grain rotation in thin films of gold. Acta Mater 46:2623–2633. https://doi.org/10.1016/S1359-6454(97)00467-9

[45] Moldovan D, Yamakov V, Wolf D, Phillpot SR (2002) Scaling behavior of grain-rotation-induced grain growth. Phys Rev Lett 89:206101. https://doi.org/10.1103/PhysRevLett.89.206101

[46] Raj R, Ashby MF (1971) On grain boundary sliding and diffusional creep. Metall Trans 2:1113–1127. https://doi.org/10.1007/BF02664244

[47] Lifshitz IM (1963) On the theory of diffusion-viscous flow of polycrystalline bodies. J Exp Theor Phys 17:909–920

[48] Langdon TG (2006) Grain boundary sliding revisited: developments in sliding over four decades. J Mater Sci 41:597–609. https://doi.org/10.1007/s10853-006-6476-0

[49] Rachinger WA (1952) Relative grain translations in the plastic flow or aluminium. J Inst Met 81:33–41

[50] Obara T, Yoshinga H, Morozumi S (1973) {11$\bar{2}$2}〈1123〉 Slip system in magnesium. Acta Metall 21:845–853. https://doi.org/10.1016/0001-6160(73)90141-7

[51] Zolotoyabko E (2011) Basic Concepts of Crystallography. Wiley VCH, Weinheim

[52] Murray JL (1982) The Al−Mg (Aluminum−Magnesium) system. Bull Alloy Phase Diagr 3:60–74. https://doi.org/10.1007/BF02873413

[53] Hutchinson CR, Nie JF, Gorsse S (2005) Modeling the precipitation processes and strengthening mechanisms in a Mg-Al-(Zn) AZ91 alloy. Metall Mater Trans A 36:2093–2105. https://doi.org/10.1007/s11661-005-0330-x

[54] Doneghan M, Heald PT (1975) An empirical interatomic potential for defect calculations in magnesium. Phys Status Solidi A 30:403–408. https://doi.org/10.1002/pssa.2210300143

[55] Sahoo D, Sahu HK (1978) Lattice distortion around a vacancy in magnesium. Phys Rev B 18:6738–6743. https://doi.org/10.1103/PhysRevB.18.6738

[56] Chetty N, Weinert M, Rahman TS, Davenport JW (1995) Vacancies and impurities in aluminum and magnesium. Phys Rev B 52:6313–6326. https://doi.org/10.1103/PhysRevB.52.6313

[57] Čížek J, Janeček M, Vlasák T et al (2019) The development of vacancies during severe plastic deformation. Mater Trans 60:1533–1542. https://doi.org/10.2320/matertrans.MF201937

[58] Ungár T, Schafler E, Hanák P et al (2005) Vacancy concentrations determined from the diffuse background scattering of X-rays in plastically deformed copper. Int J Mater Res 96:578–583. https://doi.org/10.3139/ijmr-2005-0103

[59] Shi H, Huang Y, Luo Q et al (2022) A short review on diffusion coefficients in magnesium alloys and related applications. J Magnes Alloys 10:3289–3305. https://doi.org/10.1016/j.jma.2022.12.003

[60] Schaefer H-E (1987) Investigation of thermal equilibrium vacancies in metals by positron annihilation. Phys Status Solidi A 102:47–65. https://doi.org/10.1002/pssa.2211020104

[61] Springer T (1972) Quasielastic neutron scattering for the investigation of diffusive motions in solids and liquids. In: Höhler G (ed) Springer tracts in modern physics, vol 64. Springer, Berlin, pp 1–100

[62] Petry W, Vogl G (1987) Potential and limits of nuclear methods in diffusion studies. Mater Sci Forum

15–18:323–348. https://doi.org/10.4028/www.scientific.net/MSF.15-18.323

[63] Vogl G (1999) Recent studies on diffusion in intermetallics by mossbauer spectroscopy and nuclear resonant scattering of synchrotron radiation. High Temp Mater Process 18:293–304. https://doi.org/10.1515/HTMP.1999.18.5-6.293

[64] Yoshida Y, Langouche G (2021) Modern Mössbauer spectroscopy: new challenges based on cutting-edge techniques. Springer, Singapore. https://doi.org/10.1007/978-981-15-9422-9

Publisher's Note Springer Nature remains neutral with regard to jurisdictional claims in published maps and institutional affiliations.